

High-throughput discovery and electron-doping tuning of superconducting ternary lithium borides

Bohan Cao(曹博瀚), Xinwei Wang(王新伟), Yibo Sun(孙一博), Mengxin Yang(杨孟鑫), Defang Duan(段德芳), Fubo Tian(田夫波), and Tian Cui(崔田)

Citation: Chin. Phys. B, 2026, 35 (**3**): 037401. DOI: 10.1088/1674-1056/ae27b1
http://cpb.iphy.ac.cn; http://iopscience.iop.org/cpb

What follows is a list of articles you may be interested in

Doping-dependent optical properties in YBCO superconducting films via $BaHfO_3$ nanocrystal addition

Shulun Han(韩淑伦), Yuanjie Ning(宁苑杰), Jing Chen(陈静), Yanqun Guo(郭艳群), Zicong Yang(杨子聪), Ping Zhu(朱萍), Zhigang Zeng(曾志刚), Chuanbing Cai(蔡传兵), Xinmao Yin(尹鑫茂), and Lijun Tian(田立君)
Chin. Phys. B, 2026, 35 (**2**): 027404. DOI: 10.1088/1674-1056/adee87

Exotic superconductivity in new topological kagome metal $CsTi_3Bi_5$

Jiali Liu(刘家利), Zhen Zhao(赵振), Hongqin Xiao(肖洪钦), Yuhang Zhang(张宇航), Zouyouwei Lu(鲁邹有为), Jihu Lu(卢佶虎), Feng Wu(吴凤), Chengjie Xu(徐诚杰), Hua Zhang(张华), Hui Chen(陈辉), Haitao Yang(杨海涛), Ziyi Liu(刘子儀), Xiaoli Dong(董晓莉), and Hongjun Gao(高鸿钧)
Chin. Phys. B, 2026, 35 (**2**): 027403. DOI: 10.1088/1674-1056/ae2c6d

Pressure-induced superconductivity in kagome metal $CsCr_3Sb_5$: Role of spin-orbit coupling and inter-orbital spin fluctuations

Wei Wang(王巍), Shun-Li Yu(于顺利), and Jian-Xin Li(李建新)
Chin. Phys. B, 2026, 35 (**2**): 027401. DOI: 10.1088/1674-1056/ae23ae

Pressure-stabilized Li_2K electride with superconducting behavior

Xiao-Zhen Yan(颜小珍), Quan-Xian Wu(邬泉县), Lei-Lei Zhang(张雷雷), and Yang-Mei Chen(陈杨梅)
Chin. Phys. B, 2025, 34 (**9**): 097405. DOI: 10.1088/1674-1056/add009

Superconductivity and band topology of double-layer honeycomb structure M_2N_2 (M = Nb, Ta)

Jin-Han Tan(谭锦函), Na Jiao(焦娜), Meng-Meng Zheng(郑萌萌), Ping Zhang(张平), and Hong-Yan Lu(路洪艳)
Chin. Phys. B, 2025, 34 (**9**): 097402. DOI: 10.1088/1674-1056/adee04

SPECIAL TOPIC — Structures and properties of materials under high pressure

High-throughput discovery and electron-doping tuning of superconducting ternary lithium borides

Bohan Cao(曹博瀚)[1], Xinwei Wang(王新伟)[1], Yibo Sun(孙一博)[1], Mengxin Yang(杨孟鑫)[1], Defang Duan(段德芳)[1], Fubo Tian(田夫波)[1,†], and Tian Cui(崔田)[2,1,‡]

[1] *State Key Laboratory of High Pressure and Superhard Materials, College of Physics, Jilin University, Changchun* 130012, *China*
[2] *School of Physical Science and Technology, Ningbo University, Ningbo* 315211, *China*

(Received 18 September 2025; revised manuscript received 17 November 2025; accepted manuscript online 4 December 2025)

Incorporating another metal into binary metal borides has emerged as a highly effective strategy for optimizing material properties. Herein, using high-throughput calculations, we systematically investigated the structural, electronic, and superconducting properties of $Fm\bar{3}m$ and $F\bar{4}3m$ phases of Li_2MB (M = alkaline earth, 3d, and 4d metals). Our analysis of 48 Li_2MB compounds at 0–60 GPa reveals that four of them are promising superconductors with $T_C \geq 10$ K. It is further demonstrated that substitution of different M elements serves as an effective strategy for electron doping, enabling precise control of the band structure and density of states near the Fermi level for the $F\bar{4}3m$ phase. This behavior is exemplified in $Li_2Sc_{1-x}Ti_xB$ ($x = 0.05$–0.25), which transforms from a semiconductor into a metal and further into a superconductor with increasing Ti doping concentration. For the $Fm\bar{3}m$ phase, Dirac points near the Fermi level are observed in the M = Sc and Y systems, suggesting unique electronic behavior. Our work provides deep insight into the superconducting mechanisms of lithium-based borides and offers guidance for the targeted design of novel boride superconductors.

Keywords: high-through calculations, borides, superconductivity, electronic doping

PACS: 74.25.–q, 71.20.–b, 63.20.dk

DOI: 10.1088/1674-1056/ae27b1 **CSTR:** 32038.14.CPB.ae27b1

1. Introduction

Boron occupies a unique position on the periodic table, residing at the boundary between metals and nonmetals. This duality endows it with the ability to both donate and accept electrons, enabling rich and varied bonding behavior. Consequently, boron forms complex allotropes and, upon reaction with metals, generates diverse structural frameworks including two-dimensional (2D) layered networks and three-dimensional (3D) boron cages. These structures impart borides with outstanding properties, including high hardness, superconductivity, high melting points, and unique electrical conductivity, making them an ideal platform for the design of advanced functional materials.[1–13]

Transition metals (TMs), with their high valence-electron densities, easily form compounds with light elements such as boron, yielding materials with remarkable properties. For example, MoB_2 exhibits superconductivity under high pressure with a critical temperature $T_C \sim 32$ K at 100 GPa, the second highest T_C reported for any boride;[14–16] ZrB_{12} combines high hardness with metallic conductivity (resistivity $\rho \approx 18$ μΩ);[17] monoclinic MnB_4 is identified as a superhard phase with a theoretical hardness of 49.9 GPa[18] and shows superconductivity up to 14.2 K[19] under pressure.

Introducing a third metal into binary metal borides effectively optimizes their properties. In particular, the introduction of Li atoms into binary metal–boron compounds to form ternary Li–M–B systems has attracted considerable attention. For example, the insertion of Li into the Mg–B system yields ternary Li–Mg–B metastable layered phases with a superconducting critical temperature (T_C) 10%–20% higher than that of MgB_2 (39 K);[20] Li insertion into the superconducting clathrate LaB_8 system yields the ternary $LiLaB_8$ metastable phase featuring a double-cage boron framework, which concurrently exhibits nontrivial band topology;[21] the introduction of Li into the Mn–B system yields the ternary Li_2MnB_8 demonstrating superconductivity with an estimated T_C of 15 K at 50 GPa;[22] studies on Li–Co–B and Li–Ni–B systems have revealed that at ambient pressure, the ground-state Li_2CoB[23] and Li_2NiB[24] are both promising potential anode materials for lithium-ion batteries. Kolmogorov *et al.*[25] demonstrated that a number of Li–M–B (M = alkali metals and transition metals) systems gain in stability with respect to LiB and MB_2. In the $Li_{2(1-x)}M_xB_2$ ternary compounds, some boron states remain hole-doped, which can induce MgB_2-type superconductivity.

Inspired by this, we investigated the Li_2MB (M = alkaline earth metals, 3d, and 4d transition metals) systems. Our focus on this stoichiometry is motivated by the lack of research

†Corresponding author. E-mail: tianfb@jlu.edu.cn
‡Corresponding author. E-mail: cuitian@jlu.edu.cn

© 2026 Chinese Physical Society and IOP Publishing Ltd. All rights, including for text and data mining, AI training, and similar technologies, are reserved.

on low-boron ternary phases compared to boron-rich phases. We first performed a detailed structural search for Li_2ScB and Li_2YB, revealing that both exhibit unusual cubic phases under high pressure. Based on this discovery, we then conducted an in-depth study of these cubic Li_2MB structures using high-throughput calculations.

2. Methods

We employed the evolutionary algorithm, as implemented in the USPEX code, to conduct structural searches at 0–60 GPa.[26–28] Our structure searches used system sizes of 1–4 formula units (f.u.) per simulation cell. Each generation contained 80 structures, and 30–50 generations were performed to achieve convergence. Structural optimization and electronic property calculations were performed within the Vienna *ab-initio* simulation package (VASP), employing density functional theory (DFT).[29,30] The Perdew–Burke–Ernzerhof (PBE) functional of the generalized gradient approximation was employed to describe the exchange and correlation energy of electrons.[31] To model the interactions between the ionic cores and valence electrons, the scalar relativistic projector augmented wave (PAW) method was used.[32] The cutoff energy of 700 eV and Monkhorst–Pack k meshes with a grid spacing of $2\pi \times 0.02$ Å^{-1} were set to ensure that the enthalpy converges to 1 meV/atom. Phonon calculations were performed using PHONOPY with a $2 \times 2 \times 2$ supercell containing 128 atoms[33] and the QUANTUM ESPRESSO (QE) package.[34] The superconducting properties were calculated based on density functional perturbation theory with ultrasoft pseudopotentials[35,36] in the QE code. The kinetic energy cutoff was set to 80 Ry, and the charge density cutoff of the plane wave basis was chosen to be 880 Ry. The k-mesh and the q-mesh were set to $24 \times 24 \times 24$ and $4 \times 4 \times 4$, respectively.

3. Result

The stability relationships are clear from Figs. 1(a) and 1(b), which summarize the energies of various structures of Li_2ScB and Li_2YB. The stable ground-state Li_2ScB is the $R\bar{3}m$ phase below 8 GPa, transitioning to the *Cmcm* phase in the 8–32 GPa range. Above 32 GPa, the face-centered cubic (fcc) Li_2ScB becomes the stable ground state, with the $F\bar{4}3m$ phase stable from 32 GPa to 38 GPa, followed by the $Fm\bar{3}m$ phase from 38 GPa to 60 GPa. In contrast to Li_2ScB, the ground-state phase of Li_2YB is the *Cmcm* phase below 35 GPa, transitioning to the $Fm\bar{3}m$ phase between 35 GPa and 60 GPa. The $F\bar{4}3m$ phase remains metastable throughout the 0–60 GPa pressure range. Considering the abundant precursors,[37–43] we systematically investigated the possible synthetic routes for Li_2ScB and Li_2YB. Li_2ScB remains enthalpically unstable with respect to decomposition into Li, Sc, and ScB_2 among the synthetic routes considered below approximately 43 GPa, as shown in Fig. 1(c). In contrast, for Li_2YB, increasing pressure does not lead to a straightforward stabilization. Instead, it induces a shift in the dominant decomposition pathway from $2Li + 1/2Y + 1/2YB_2$ at low pressure toward $Y + Li_2B$ at higher pressures (Fig. 1(d)). Figure 1(e) shows that Li_2ScB lies on the ternary convex hull, demonstrating energetic stability against decomposition into the stable binary phases located at the convex-hull edge at 60 GPa with the inclusion of zero-point energy (ZPE), while Li_2YB is about 0.073 eV/atom above the convex hull, as shown in Fig. 1(f), with ZPE. Our detailed investigations of Li_2ScB and Li_2YB reveal a fascinating pressure-induced stabilization of cubic phases. Given the intriguing behavior of Li_2ScB and Li_2YB under high pressure, we now extend this investigation to other systems, specifically Li_2MB (M = transition metals and alkaline earth metals) using high-throughput computational screening.

Figure 2(a) displays the two cubic structures of Li_2MB with space groups $F\bar{4}3m$ and $Fm\bar{3}m$. In the $F\bar{4}3m$ phase, there are two distinct Li positions in the conventional cell of Li_2MB, namely, Li_1 (0.500, −0.500, 0.500) and Li_2 (0.250, −0.250, 0.250). Li_1 atoms and their adjacent B atoms form tetrahedral coordination, while the Li_1–B sublattice constitutes a diamond structure. Similarly, Li_2 atoms and their adjacent M atoms form tetrahedral coordination, while the Li_2–M sublattice also constitutes a diamond structure. Thus, the $F\bar{4}3m$ Li_2MB compound can be viewed as comprising two interpenetrating diamond structures. In contrast to the $F\bar{4}3m$ phase, the high-pressure $Fm\bar{3}m$ phase can be viewed as dual NaCl-type frameworks. Here, Li atoms occupy one NaCl cubic sublattice, while the M–B network constitutes another isostructural framework.

We evaluated the dynamical stability of Li_2MB in the pressure range of 0–60 GPa using phonon calculations shown in Fig. 2(b) (the phonon dispersions are shown in Figs. S1 and S9). The phonon stability for each phase, indicated by circles ($F\bar{4}3m$) and squares ($Fm\bar{3}m$), is plotted at 0 (left), 30 (middle), and 60 GPa (right) within each elemental cell. It can be observed that the $Fm\bar{3}m$ Li_2MB phase is dynamically unstable at 0 GPa, whereas only approximately 10 metals (M = Mg, Ca, Sc, Ti, Cu, Zn, Y, Zr, Ag, Cd) forming $Fm\bar{3}m$ Li_2MB become dynamically stable as pressure increases. For the $F\bar{4}3m$ Li_2MB phase, dynamical instability persists across the 0–60 GPa pressure range for only five metals (M = Ca, Sr, Nb, Mo, Ru). Given the stabilization of cubic structures in Li_2MB (M = Sc, Y) under high pressure, the relative stability of these phases at 60 GPa was evaluated for other M atoms using the calculated formation enthalpies $\Delta H = [H(Li_2MB) - H(LiB) - H(Li) - H(M)]/4$ shown in Fig. 2(c). Here $H(Li_2MB)$ is the total enthalpy of Li_2MB at 60 GPa, and $H(LiB)$, $H(Li)$, and $H(M)$ are the enthalpies of LiB, Li, and M

metal at 60 GPa. Based on computational screening, only dynamically stable structures were considered, along with those potentially energetically stable or metastable (formation energies < 50 meV/atom). Furthermore, the $Fm\bar{3}m$ structure is generally less stable than $F\bar{4}3m$ across the Li_2MB series. Remarkably, this trend is inverted for five elements (M = Sc, Y, Ca, Sr, Mg), with $Fm\bar{3}m$ showing lower formation energies.

Having established the energetic and dynamical stability, we now turn to the electronic properties. These compounds display remarkably diverse electronic behavior, ranging from semiconductors to high-density of states (DOS) metals, tunable by the choice of the M element. Our calculations reveal that $F\bar{4}3m$ Li_2ScB and Li_2YB are semiconductors whose band gaps exhibit a notable nonmonotonic dependence on pressure, initially increasing before decreasing under compression, as shown in Fig. 3(a). The band structures are available in Fig. S2. Previous studies have suggested that this phenomenon may be related to chemical bonding.[44] To further investigate, taking Li_2ScB as an example, we calculated the electron localization function (ELF) for Li_2ScB, as shown in Fig. 3(b). Figure 3(b) displays the ELF of the $F\bar{4}3m$ phase Li_2ScB at 0 GPa. Distinct electron accumulation around B atoms and electron depletion near Li and Sc atoms are observed, indicating the formation of Li–B and Sc–B ionic bonds.

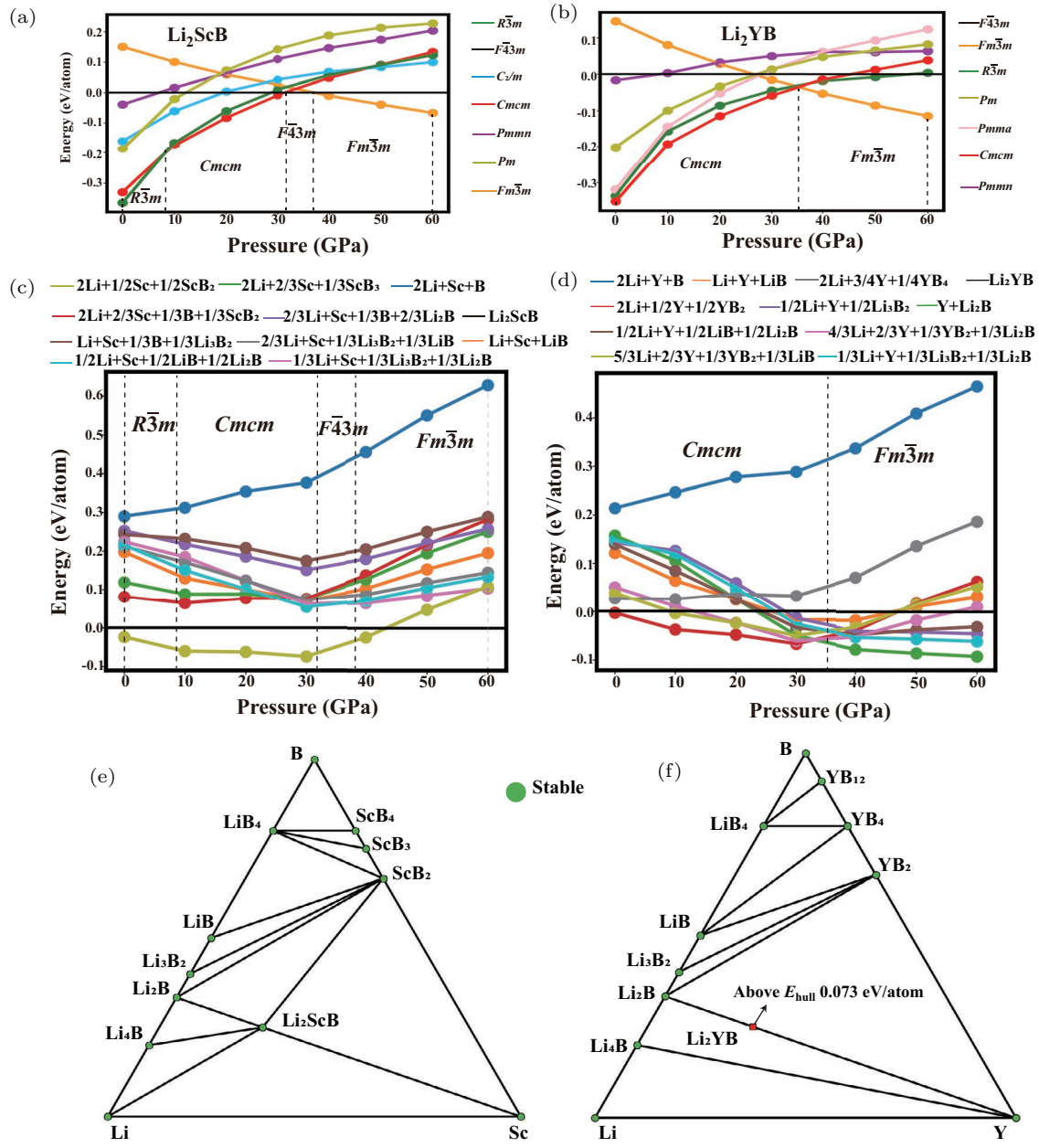


Fig. 1. Energy differences of various phases in (a) Li_2ScB and (b) Li_2YB relative to the $F\bar{4}3m$ phase within the pressure range of 0–60 GPa. (c) Decomposition enthalpies of Li_2ScB into the elements Li, Sc, and B and possible binary compounds, Sc–B and Li–B, at 0–60 GPa. (d) Decomposition enthalpies of Li_2YB into the elements Li, Y, and B and possible binary compounds, Y–B and Li–B, at 0–60 GPa. Convex hulls of the formation energies with the inclusion of ZPE for (e) Li_2ScB and (f) Li_2YB based on previously reported phases at 60 GPa. Stable compositions are indicated as green circles; metastable compositions are indicated as red squares.

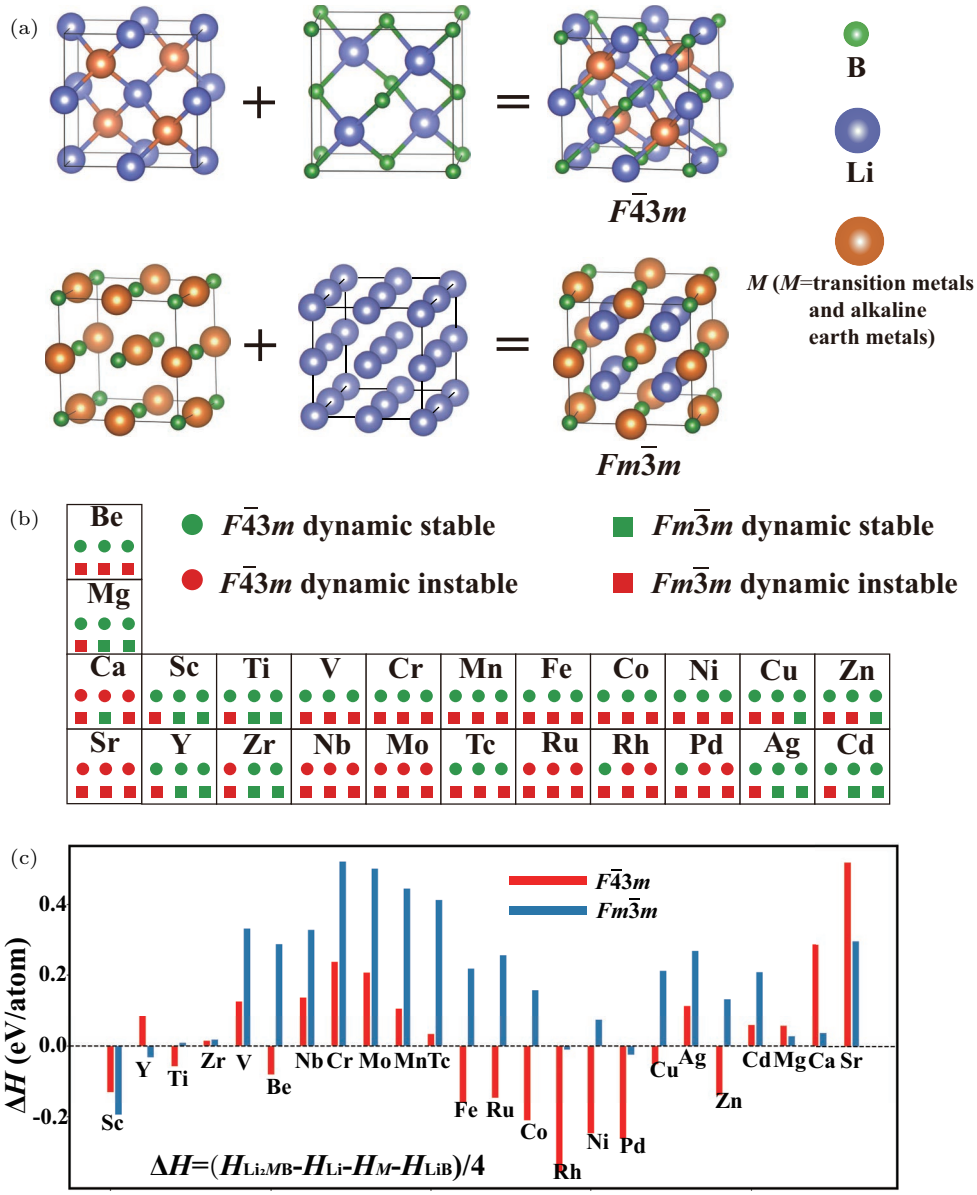


Fig. 2. (a) Structures of the $F\bar{4}3m$ and $Fm\bar{3}m$ phases. (b) Phonon dispersion curves from high-throughput calculations at pressures of 0 GPa, 30 GPa, and 60 GPa, from left to right. (c) Formation enthalpies from high-throughput calculations at 60 GPa.

Notably, significant electron aggregation occurs between the labeled Li_1 and B atoms, resulting from simultaneous electron transfer to B from both the Li_1 atom and adjacent Sc atoms. Furthermore, this electron distribution becomes distorted under the Coulomb attraction of surrounding cations, driving electrons originally localized around B atoms toward the Li_1 site, thereby inducing a shift from ionic to covalent-like bonding in the Li_1–B bond.

Figure 3(c) illustrates the position-dependent evolution of the ELF values across the Li_1–B bond in $F\bar{4}3m$ Li_2ScB. At 0 GPa, the ELF value between Li_1 and B reaches a maximum of approximately 0.8, approaching covalent-bond-like characteristics. As the pressure increases from 0 GPa to 30 GPa, the atomic distance decreases, and the ELF value at the midpoint of Li_1–B bonds increases significantly (from 0.808 to 0.828). This enhancement in electron localization strengthens the covalent-like character of the Li_1–B bond. Consequently, the increased electron localization under pressure results in a widening of the band gap, as evidenced by the increase in the band gap of Li_2ScB in the pressure range of approximately 0–30 GPa shown in Fig. 3(a). However, as the pressure increases from 30 GPa to 60 GPa, despite the further reduction in the distance between Li_1 and B atoms, their ELF value changes only slightly (from 0.828 to 0.833), indicating that the enhancement of electron localization begins to saturate in this higher-pressure regime. Consequently, band broadening, induced by enhanced orbital overlap due to the reduced lattice constant, becomes the dominant factor, thereby reducing the band gap, as illustrated by the decrease in the band gap of Li_2ScB at 30–60 GPa shown in Fig. 3(a). For Li_2YB, the band gap increases in the pressure range 0–10 GPa but decreases between 10 GPa and 40 GPa. A Wilson transition from a semi-

conductor to a metal occurs at approximately 42 GPa. The corresponding ELF values are presented in Fig. S3.

The electronic band structures and DOS for compounds with M = Y, Zr, Nb, and Mo are presented in Fig. 3(d). DOS analysis reveals that the electronic states near the Fermi level are dominated by contributions from the M atom. Interestingly, for M elements residing in the same period of the periodic table, the number of valence electrons increases with atomic number, demonstrating the electron doping effect, as shown in Fig. 3(d). Notably, the energy region of the bands near the Fermi level in Li_2YB lies approximately 0.8 eV below the Fermi level in Li_2ZrB, roughly 1.8 eV below in Li_2NbB, and 2.3 eV below in Li_2MoB. A corresponding downward shift of the same spectral weight is observed in the DOS plots. This phenomenon can be understood as the additional electrons raising the Fermi energy, which shifts the electronic bands and density of states near the Fermi level. Consequently, substituting the M element provides an effective and tunable means of electron doping, allowing precise control over the band structure and the density of states near the Fermi level.

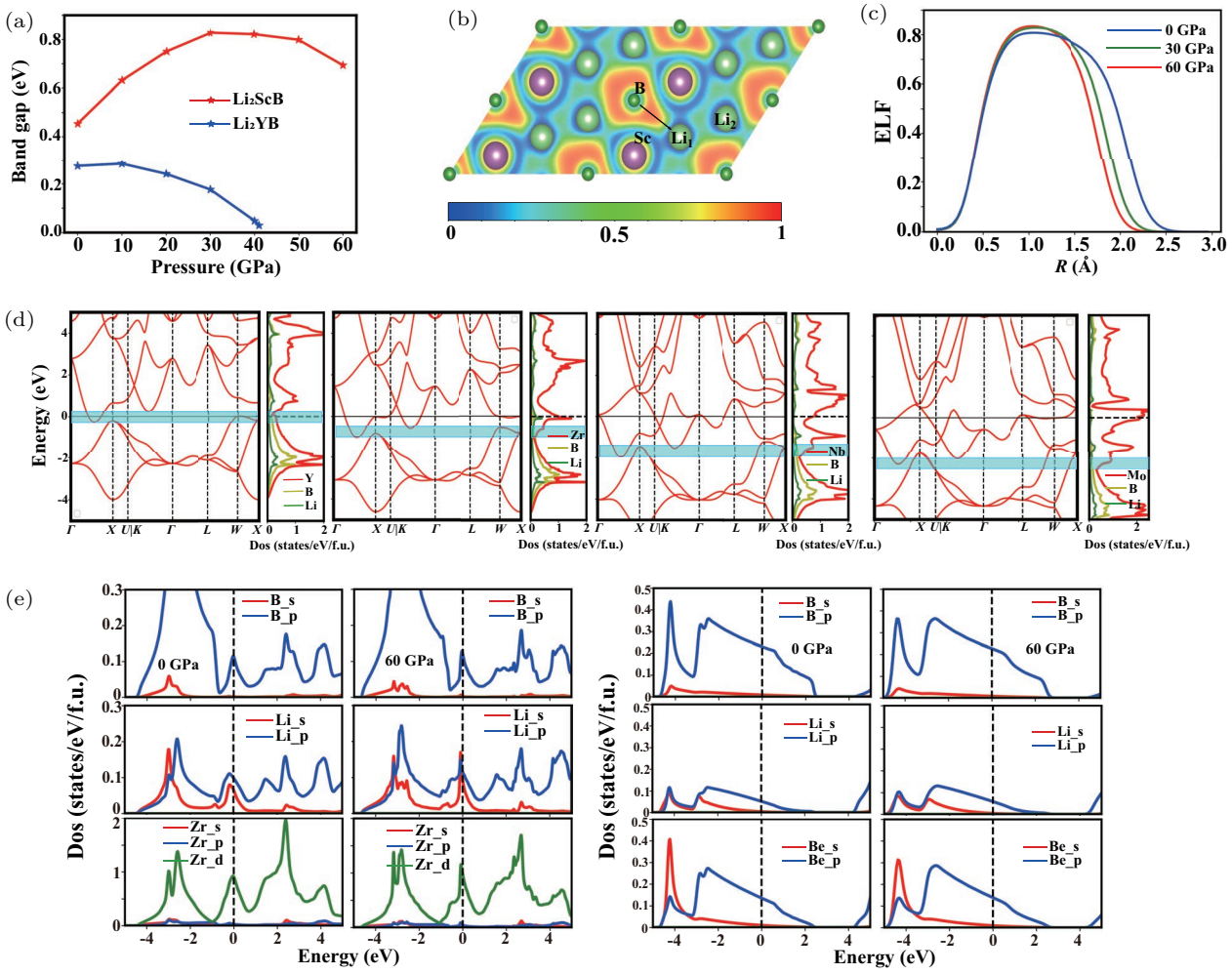


Fig. 3. (a) Band gaps of $F\bar{4}3m$ Li_2ScB and Li_2YB within the pressure range of 0–60 GPa. (b) ELF of $F\bar{4}3m$ Li_2ScB on the (1 −1 0) plane at 0 GPa. (c) ELF values across the B–Li_1 bond along the line shown in (b). (d) Band structures and DOS of Li_2YB, Li_2ZrB, Li_2NbB, and Li_2MoB at 60 GPa. PDOS of (e) Li_2ZrB and (f) Li_2BeB.

The projected DOS (PDOS) of $F\bar{4}3m$ Li_2MB (M = Zr, Be) at 0 GPa and 60 GPa is presented in Figs. 3(e) and 3(f). (The DOS at the Fermi level for $F\bar{4}3m$ Li_2MB without spin polarization is shown in Fig. S4. The spin-polarized DOS for Li_2MB compounds, where M denotes a transition metal, is provided in Fig. S5.) As shown in Fig. 3(e), for Li_2ZrB, the Zr d orbitals dominate the DOS at the Fermi level under both 0 GPa and 60 GPa, followed by B p orbitals. Contributions from Li s and p orbitals are the smallest, with the Li p orbitals being comparable to B p orbitals. As pressure increases, the contributions from Zr d and Li s/p orbitals at the Fermi level increase. In contrast, for Li_2BeB, the Fermi-level DOS is dominated by B p orbitals, while Li p orbitals make the smallest contribution and all s-orbitals are negligible. The PDOS of $Fm\bar{3}m$ Li_2CaB at 30 GPa is shown in Fig. S6.

The $Fm\bar{3}m$ phase of Li_2MB becomes energetically favorable over $F\bar{4}3m$ only for M = Sc, Y, Ca, and Mg, concurrently exhibiting negative formation enthalpies with respect to decomposition into LiB, M, and Li. Therefore, the following discussion of electronic properties focuses primarily

on M = Sc and Y. We plotted the electronic band structures and 3D valence and conduction band surfaces to analyze the electronic characters of $Fm\bar{3}m$ phase Li_2ScB (Figs. 4(a) and 4(b)) at 60 GPa, and the band structure of Li_2YB is shown in Fig. S7 at 35 GPa. Two frustrated Dirac cones are observed around the Γ point near the Fermi level. One cone is located at an off-symmetry point between Γ and X, denoted as the D point with a 3 meV band gap, while the other lies along the K–Γ path, exhibiting a 12 meV gap denoted as the Q point. The two frustrated Dirac cones are characterized by compensated electron-hole pockets. For both Li_2ScB and Li_2YB, the Dirac cones are gapped under spin-orbit coupling (SOC), with gaps exceeding 100 meV, as shown in Figs. 4(c) and S7.

To further understand the contributions of the two Dirac cones, the projected band structures of Li_2ScB and Li_2YB are plotted in Figs. 4(d) and S8, respectively. In Fig. 4(d), for the p and d orbitals, the radii of the colored lines are proportional to the corresponding orbital contributions. The results suggest that the D Dirac point mainly originates from the d_{xy} and d_{xz} orbitals of Sc atoms, as well as the p_x orbitals of B and Li atoms. The Q Dirac point mainly arises from the $d_{x^2-y^2}$ and d_{yz} orbitals of Sc atoms hybridized with the p_y orbitals of B and Li atoms. The d_{z^2} orbitals of Sc and p_z orbitals of Li and B contribute negligibly to the Q Dirac cone.

The calculated superconducting transition temperatures (T_C) using the Allen–Dynes modified McMillan equation[45] with a typical Coulomb pseudopotential $\mu^* = 0.1$ for Li_2MB at 0 GPa, 30 GPa, and 60 GPa are shown in Fig. 5(a). Dynamically unstable structures or those with formation enthalpies $\Delta H > 50$ meV were not considered for superconductivity and are marked with a cross. Our calculations identify several promising compounds with T_C above 10 K for further research, namely Li_2BeB (0 GPa), Li_2CaB (30 GPa), Li_2ZrB (30 GPa and 60 GPa), and Li_2PdB (0 GPa).

The λ_{qv}-weighted phonon dispersions, Eliashberg spectral function $\alpha^2F(\omega)$, and integrated $\lambda(\omega)$ were calculated to evaluate the superconducting properties. At 0 GPa, the calculated T_C for $F\bar{4}3m$ Li_2BeB is 13.8 K, with a total electron–phonon coupling strength of $\lambda = 0.68$, as shown in Fig. 5(b). Analysis reveals a peak in the Eliashberg spectral function within the medium-frequency region of 8–12 THz, which contributes approximately 35% of the total λ and originates from the coupled vibrations of Li, Be, and B atoms. In the low-frequency region (0–8 THz), the contribution is 39%, whereas the high-frequency region (12–20 THz) contributes the least, approximately 26%.

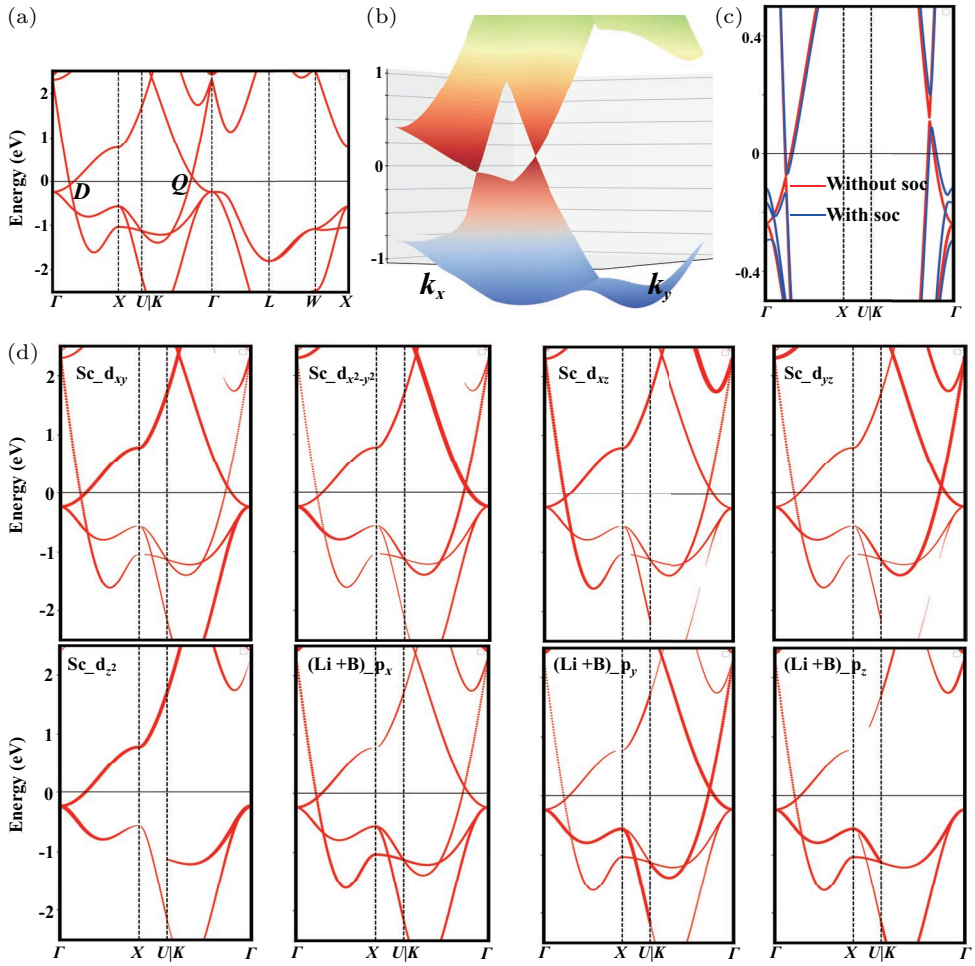


Fig. 4. (a) Electronic band structures and (b) 3D valence and conduction bands of $Fm\bar{3}m$ Li_2ScB at 60 GPa. (c) Electronic band structures of $Fm\bar{3}m$ Li_2ScB including SOC. (d) Electronic band projection structures of $Fm\bar{3}m$ Li_2ScB.

(a)

	$F\bar{4}3m$ T_c (K)			$Fm\bar{3}m$ T_c (K)		
Be	13.8	2.4	<1	×	×	×
Mg	×	×	×	×	<1	<1
Ca	×	×	×	×	16.4	×
Sc	semiconductor			<1	<1	<1
Y	semiconductor		8.6	<1	<1	<1
Ti	7.1	8.1	8.3	×	×	2.5
Zr	×	14.0	16.8	×	×	8.3
Fe	2.5	1.0	<1	×	×	×
Co	3.7	2.1	2.9	×	×	×
Rh	9.7	×	×	×	×	×
Ni	6.3	4.4	4.0	×	×	×
Cu	8.3	1.7	1.1	×	×	×
Zn	2.9	<1	<1	×	×	×
Pd	13.4	×	×	×	×	×
P (GPa)	0	30	60	0	30	60

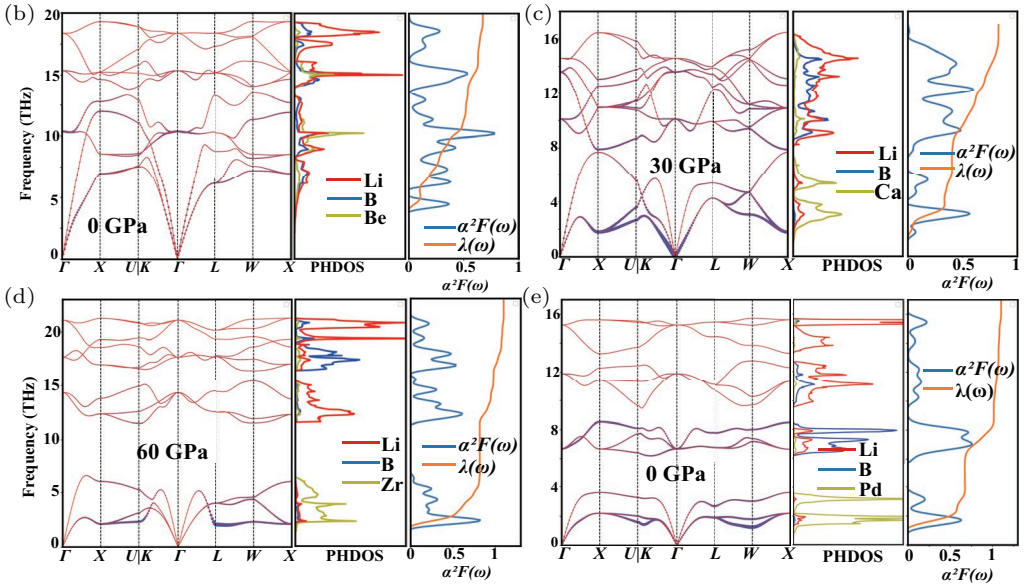


Fig. 5. (a) Results of high-throughput calculations of the superconducting transition temperature (T_C) for Li_2MB at 0 GPa, 30 GPa, and 60 GPa. Phonon dispersions with the size of blue spheres denoting the contributions to electron–phonon coupling (EPC), phonon density of states (PHDOS), Eliashberg spectral function $\alpha^2F(\omega)$, and EPC parameter $\lambda(\omega)$ for (b) $F\bar{4}3m$ Li_2BeB at 0 GPa, (c) $Fm\bar{3}m$ Li_2CaB at 30 GPa, (d) $F\bar{4}3m$ Li_2ZrB at 60 GPa, and (e) Li_2PdB at 0 GPa.

Notably, the phonon spectrum of $Fm\bar{3}m$ Li_2CaB at 30 GPa exhibits pronounced softening in the low-frequency region (0–3 THz) along the X–$U|K$ and L–W–X paths in reciprocal space, as seen in Fig. 5(c). In these regions of phonon dips, significant enhancement of electron–phonon coupling is observed, evidenced by deeper blue shades in the phonon dispersion curves. A pronounced peak in $\alpha^2F(\omega)$ contributes approximately 40% to the total electron–phonon coupling strength ($\lambda = 0.88$). Analysis of the PHDOS reveals that vibrations of Ca atoms dominate in this region. The intermediate-frequency region (3–7 THz) contributes only $\sim 9\%$ to the total λ, whereas the high-frequency region (7–16 THz), dominated by Li and B vibrations, accounts for approximately 51%.

Similar behavior is observed for Li_2ZrB and Li_2PdB, which exhibit phonon softening along the X–$U|K$ and L–W–X paths in their low-frequency regions (0–6 THz for Li_2ZrB and 0–4 THz for Li_2PdB), enhancing the electron–phonon coupling (Figs. 5(d) and 5(e)). However, in contrast to Li_2CaB and Li_2BeB, the larger atomic mass of Zr and Pd introduces a gap between acoustic and optical phonon branches, allowing a natural distinction between the acoustic branch electron–phonon coupling constant (λ_{ac}) and the optical branch coupling constant (λ_{opt}). For Li_2ZrB, $\lambda_{ac} \approx 0.82$, accounting for about 80% of the total λ, while high-frequency optical phonons (10–21 THz) contribute $\lambda_{opt} = 0.20$ (20% of total λ). In Li_2PdB, $\lambda_{ac} = 0.66$ accounts for 60% of total λ. As previously discussed, the dominant contribution to λ arises from interactions between Zr d-electrons and Zr atom vibrations. Interestingly, Fig. 5(a) shows that T_C of Li_2ZrB increases under pressure,

likely due to enhanced Zr d-orbital contribution to the DOS at the Fermi level. For Li_2PdB, intermediate-frequency optical phonons (5–9 THz) contribute approximately 35% to λ.

In Li_2MB compounds, heavier M atoms induce phonon softening in the low-frequency acoustic branches, contributing over 50% of total electron–phonon coupling. This trend is further supported by Li_2MB (M = Cu, Rh, Ni, Ti), as shown in Fig. S9, all exhibiting T_C in the 5–10 K range.

To examine the effect of electron doping on electronic properties, the virtual crystal approximation (VCA) was employed to construct $F\bar{4}3m$ $Li_2Sc_{1-x}Ti_xB$ ($x = 0.05$–0.25). Sc and Ti were selected because they are adjacent in the periodic table, both Li_2ScB and Li_2TiB are dynamically stable, and their DOS at the Fermi level differs significantly. Figure 6(a) shows that increasing Ti concentration raises the DOS at the Fermi level, transforming Li_2ScB from a semiconductor into a metal and further into a superconductor.

Figure 6(b) compares the phonon spectra and $\alpha^2F(\omega)$ of $Li_2Sc_{0.85}Ti_{0.15}B$ and $Li_2Sc_{0.75}Ti_{0.25}B$. Ti doping slightly softens low-frequency phonons, resulting in a low-frequency peak in $\alpha^2F(\omega)$ and enhanced electron–phonon coupling. Consequently, $Li_2Sc_{0.75}Ti_{0.25}B$ exhibits $\lambda = 0.35$ and $T_C = 1$ K, higher than $Li_2Sc_{0.85}Ti_{0.15}B$ ($\lambda = 0.26$, $T_C = 0.1$ K). The phonon spectrum of $Li_2Sc_{0.75}Ti_{0.25}B$ calculated using the supercell approach (Fig. S10) shows no imaginary frequencies, confirming dynamical stability.

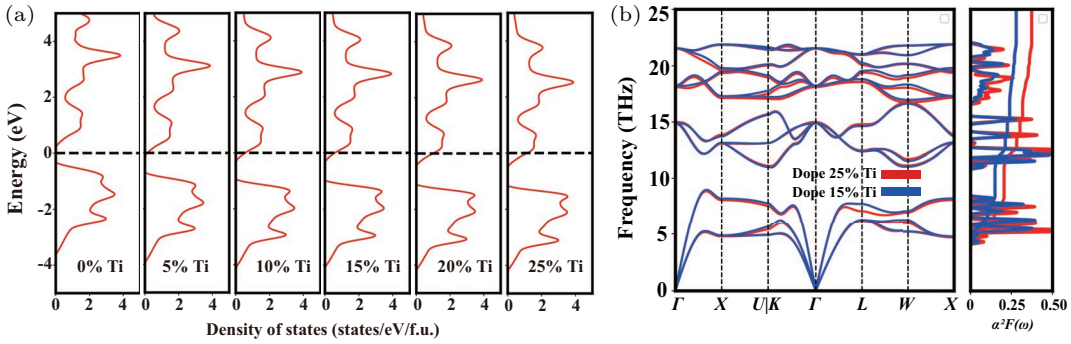


Fig. 6. (a) The DOS of $F\bar{4}3m$ $Li_2Sc_{1-x}Ti_xB$ ($x = 0.05$–0.25) at 60 GPa. (b) The phonon spectra, Eliashberg spectral function $\alpha^2F(\omega)$, and integrated $\lambda(\omega)$ of $F\bar{4}3m$ $Li_2Sc_{0.75}Ti_{0.25}B$ and $Li_2Sc_{0.85}Ti_{0.15}B$ at 60 GPa.

4. Conclusion

In summary, we conducted high-throughput calculations to explore $F\bar{4}3m$ and $Fm\bar{3}m$ Li_2MB, where M represents transition metals and alkaline earth metals. Among these metals, four potential superconducting candidates with $T_C \geq 10$ K were identified. The highest predicted T_C of 16.8 K was found in $F\bar{4}3m$ Li_2ZrB. Based on our analysis of the electronic and vibrational properties of $F\bar{4}3m$ Li_2MB, we conclude that the primary contributions to superconductivity arise from the M-derived density of states at the Fermi level and low-frequency vibrational modes.

Furthermore, substitution of the M element provides an effective and tunable strategy for electron doping, enabling precise control over the band alignment and density of states near the Fermi level. By constructing the compound $Li_2Sc_{1-x}Ti_xB$ ($x = 0.05$–0.25), we achieved a controlled evolution from a semiconductor to a metal and finally to a superconductor. For the $Fm\bar{3}m$ phase of Li_2MB, superconductivity remains relatively weak (with most transition temperatures below 1 K) among the dynamically stable M elements. Notably, the T_C of $Fm\bar{3}m$ Li_2CaB exceeds 10 K under 30 GPa. In the case of M = Sc and Y, Dirac points emerge near the Fermi level, suggesting distinctive electronic behavior in these systems. These findings enhance the understanding of superconducting mechanisms in this class of materials and facilitate the targeted exploration of novel boride compounds.

Acknowledgments

This work was supported by the National Natural Science Foundation of China (Grant Nos. 11574109 and 91745203). Parts of the calculations were performed at the High Performance Computing Center (HPCC) of Jilin University.

References

[1] Akopov G, Yeung M T and Kaner R B 2017 *Adv. Mater.* **29** 1604506
[2] Albert B and Hillebrecht H 2009 *Angew. Chem. Int. Ed. Engl.* **48** 8640
[3] Zhao B, Wang L, Tao Q and Zhu P 2023 *J. Phys. Condens. Matter* **35** 173001
[4] Carenco S, Portehault D, Boissiere C, Mezailles N and Sanchez C 2013 *Chem. Rev.* **113** 7981
[5] Gunda H, Klebanoff L E, Sharma P A, Varma A K, Dolia V, Jasuja K and Stavila V 2021 *ACS Mater. Lett.* **3** 535
[6] Han S, Yu L, Liu Y, Zhao B, Wang C, Chen X, Zhang Y, Yu R and Liu X 2023 *Adv. Funct. Mater.* **33** 2213377
[7] Yeung M T, Mohammadi R and Kaner R B 2016 *Annu. Rev. Mater. Res.* **46** 465
[8] Nagamatsu J, Nakagawa N, Muranaka T, Zenitani Y and Akimitsu J 2001 *Nature* **410** 63
[9] Medvedeva N I, Ivanovskii A L, Medvedeva J E and Freeman A J 2001 *Phys. Rev. B* **64** 020502
[10] Sevik C, Bekaert J, Petrov M and Miloševic M V 2022 *Phys. Rev. Mater.* **6** 024803
[11] Sun Y, Zhang Z, Porter A P, Kovnir K, Ho K and Antropov V 2023 *npj Comput. Mater.* **9** 204
[12] Akopov G, Yeung M T, Turner C L, Mohammadi R and Kaner R B 2016 *J. Am. Chem. Soc.* **138** 5714

[13] Bhaskar G, Gvozdetskyi V, Batuk M, Wiaderek K M, Sun Y, Wang R, Zhang C, Carnahan S L, Wu X, Ribeiro R A, Bud'ko S L, Canfield P C, Huang W, Rossini A J, Wang C, Ho K, Hadermann J and Zaikina J V 2021 *J. Am. Chem. Soc.* **143** 4213

[14] Pei C, Zhang J, Wang Q, Zhao Y, Gao L, Gong C, Tian S, Luo R, Li M, Yang W, Lu Z, Lei H, Liu K and Qi Y 2023 *Natl. Sci. Rev.* **10** nwad034

[15] Liu X, Huang X, Song P, Wang C, Zhang L, Lv P, Liu L, Zhang W, Cho J-H and Jia Y 2022 *Phys. Rev. B* **106** 064507

[16] Quan Y, Lee K-W and Pickett W E 2021 *Phys. Rev. B* **104** 224504

[17] Ma T, Li H, Zheng X, Wang S, Wang X, Zhao H, Han S, Liu J, Zhang R, Zhu P, Long Y, Cheng J, Ma Y, Zhao Y, Jin C and Yu X 2017 *Adv. Mater.* **29** 1604003

[18] Wang B, Li X, Wang Y X and Tu Y F 2011 *J. Phys. Chem. C* **115** 21429

[19] Xiang Z, Zhang Y, Lu Q, Li Q, Li Y, Huang T, Zhu Y, Ye Y, Sun J and Wen H 2025 *Adv. Mater.* **37** 2416882

[20] Kafle G P, Tomassetti C R, Mazin I I, Kolmogorov A N and Margine E R 2022 *Phys. Rev. Mater.* **6** 084801

[21] Liang Y, Zhang X, Xu M, Xu G and Li Y 2022 *Mater. Today Phys.* **27** 100817

[22] Yuan X, Zhang Y, Hao J, Xu M and Li Y 2023 *Phys. Rev. Res.* **5** 043114

[23] Sun J, Wang R, Ding Z, Zhang X, Zhang Q, Zhang B, Dong H and Wu F 2023 *Inorg. Chem.* **62** 8136

[24] Wang R, Sun Y, Gvozdetskyi V, Zhao X, Zhang F, Xu L, Zaikina J V, Lin Z, Wang C and Ho K 2020 *J. Appl. Phys.* **127** 094902

[25] Kolmogorov A N, Calandra M and Curtarolo S 2008 *Phys. Rev. B* **78** 094520

[26] Lyakhov A O, Oganov A R, Stokes H T and Zhu Q 2013 *Comput. Phys. Commun.* **184** 1172

[27] Oganov A R, Lyakhov A O and Valle M 2011 *Acc. Chem. Res.* **44** 227

[28] Oganov A R and Glass C W 2006 *J. Chem. Phys.* **124** 244704

[29] Kresse G and Furthmüller J 1996 *Comput. Mater. Sci.* **6** 15

[30] Kresse G and Furthmüller J 1996 *Phys. Rev. B* **54** 11169

[31] Perdew J, Burke K and Ernzerhof M 1996 *Phys. Rev. Lett.* **77** 3865

[32] Blochl P E 1994 *Phys. Rev. B* **50** 17953

[33] Togo A and Tanaka I 2015 *Scr. Mater.* **108** 1

[34] Giannozzi P, Baroni S, Bonini N, *et al.* 2009 *J. Phys. Condens. Matter* **21** 395502

[35] Vanderbilt D 1990 *Phys. Rev. B* **41** 7892

[36] Baroni S, de Gironcoli S, Dal Corso A and Giannozzi P 2001 *Rev. Mod. Phys.* **73** 515

[37] Kolmogorov A N and Curtarolo S 2006 *Phys. Rev. B* **74** 224507

[38] Kolmogorov A N and Curtarolo S 2006 *Phys. Rev. B* **73** 180501

[39] Rosner H and Pickett W E 2003 *Phys. Rev. B* **67** 054104

[40] Peng F, Miao M, Wang H, Li Q and Ma Y 2012 *J. Am. Chem. Soc.* **134** 18599

[41] Hermann A, McSorley A, Ashcroft N W and Hoffmann R 2012 *J. Am. Chem. Soc.* **134** 18606

[42] Qiu C, Liu S, Liu Y and Du Y 2025 *Intermetallics* **177** 108588

[43] Tao X, Yang A, Quan Y and Zhang P 2025 *Phys. Chem. Chem. Phys.* **27** 3023

[44] Sun Y, Cao B, Chen S, Wang X, Duan D, Tian F and Cui T 2024 *ACS Appl. Mater. Interfaces* **16** 60482

[45] Allen P B and Dynes R C 1975 *Phys. Rev. B* **12** 905